

1 Ecosystem Climate Sensitivities Drive the Divergence in
2 Aerosol-Induced Carbon Uptake Across CMIP6 Models

3 Zhaoyang Zhang¹, Meng Fan^{2*}, Minghui Tao³, Yunhui Tan⁴, Quan Wang⁵

4 1. College of Geography and Environmental Sciences, Zhejiang Normal University,
5 Zhejiang Province 321000, China

6 2. Aerospace Information Research Institute, Chinese Academy of Sciences, Beijing
7 100101, China

8 3. School of Geography and Information Engineering, China University of
9 Geosciences, Wuhan 430074, China

10 4. School of Computer Science, China University of Geosciences, Wuhan 430078,
11 China

12 5. Faculty of Agriculture, Shizuoka University, Shizuoka 4228529, Japan

13 *Corresponding author: Meng Fan (fanmeng@aircas.ac.cn)

14

15

16

17 **Abstract**

18 Anthropogenic aerosols significantly affect the terrestrial carbon cycle. Many
19 models have been developed to simulate the effects of aerosols on regional ecosystem
20 productivity. However, the differences among models in simulating the impacts of
21 aerosols on gross primary production (GPP) remain unclear. To investigate the response
22 of GPP to aerosol loadings among different models, we analyzed historical and hist-
23 piAer simulations from five Earth System Models (ESMs) in Coupled Model
24 Intercomparison Project Phase 6 (CMIP6). The results showed that all models captured
25 the decrease in GPP from 1850 to 2014 (mean: $-0.0586 \text{ gC m}^{-2}\text{d}^{-1}$) and the magnitudes
26 of aerosol-induced GPP changes varied greatly (-0.0234 to $-0.1151 \text{ gC m}^{-2}\text{d}^{-1}$). To
27 analyze the roles of aerosol representations and model sensitivities to climatic factors
28 across ESMs, we developed a biophysical attribution framework. Our results showed
29 that inter-model discrepancies in simulating the effects of aerosols on GPP were
30 primarily driven by the differences in ecosystem climate sensitivities across ESMs,
31 especially the response of photosynthesis to radiation and temperature. These findings
32 provide critical insights into understanding the impacts of anthropogenic aerosols on
33 the terrestrial ecosystem carbon cycle.

34 **Keywords:** gross primary production (GPP); aerosols; earth system models (ESMs);
35 CMIP6

36

37

38 **1. Introduction**

39 Terrestrial gross primary production (GPP) is the largest carbon flux in the global
40 carbon cycle (Anav et al., 2015; Lai et al., 2024). Understanding the response of GPP
41 to various environmental factors is critical for accurately simulating the photosynthesis
42 of terrestrial ecosystems (Piao et al., 2008; Huang et al., 2019). Atmospheric aerosol
43 loadings have significantly increased since the Industrial Revolution due to the
44 increased combustion of fossil fuels (Liu et al., 2022). The increased aerosol loadings
45 significantly affect the amount of solar radiation reaching the Earth's surface (Tan et al.,
46 2023), cloud properties (Manshausen et al., 2022), and regional climate (Najafi et al.,
47 2015; Leung and Van Den Heever, 2023). Aerosols also play an important role in the
48 photosynthesis of terrestrial ecosystems by altering the vegetation growing
49 environment, such as radiation and temperature (Zhang et al., 2023b; Zhang et al.,
50 2019).

51 Atmospheric aerosols can affect GPP through four pathways. First, increasing
52 aerosols can reduce the incoming radiation by absorbing and scattering sunlight (Wu et
53 al., 2025). Second, aerosol loadings also increase the fraction of diffuse radiation (DF)
54 reaching the Earth's surface. The increased DF can enhance the canopy light-use
55 efficiency (LUE) (Gu et al., 2003; Gu et al., 2002). Third, aerosols can also influence
56 the total radiation and DF reaching the surface by affecting the cloud properties (Khatri
57 et al., 2021). Furthermore, aerosols also influence the terrestrial ecosystem
58 photosynthesis through altering the air temperature and precipitation (Wang et al., 2018;
59 Zhang et al., 2021a). To quantify the effect of aerosols on GPP, ground-based
60 measurements and model simulations have been widely used.

61 Ground-based measurements provided some insights into the effect of aerosols on
62 GPP at site scale. These studies showed that the increased aerosol loadings enhanced
63 the canopy LUE by reducing the light saturation in the upper layers and enhancing
64 photosynthesis in the lower canopy layers (Gu et al., 2002; Gu et al., 2003). Niyogi et
65 al. (2004) showed that the effect of diffuse radiation induced by clouds and aerosols on
66 canopy LUE varied with the vegetation types due to the canopy structure. Ground-based

67 measurements also showed that the enhanced photosynthetic rates of sunlit and shaded
68 leaves under high aerosol loadings conditions were driven by different environmental
69 factors. The enhanced photosynthesis for sunlit and shaded leaves is induced by lower
70 vapor pressure deficit (VPD) and higher diffuse radiation, respectively (Wang et al.,
71 2018).

72 To investigate the changes of regional GPP induced by aerosols, model simulations
73 were conducted. For example, Mercado et al. (2009) and Rap et al. (2018) showed that
74 anthropogenic aerosols enhanced land carbon uptake due to the diffuse fertilization
75 effect (DFE). Yue and Unger (2017) showed that the aerosol-induced change in net
76 primary productivity (NPP) over China was from -3% to 6% depending on the local
77 aerosol optical depth (AOD). However, these studies did not account for indirect
78 aerosol radiative effects and aerosol climatic effects. To comprehensively understand
79 the impact of aerosols, many other modelling studies were conducted. For example,
80 Zhang et al. (2021a) reported that aerosols enhanced vegetation carbon dioxide sink
81 since 1850 due to the DFE and cooling effects induced by aerosols. Zhang et al. (2023a)
82 found that aerosols caused 0.43% reduction in net biome production from 1980 to 2014
83 using the Community Earth System Model (CESM, version 2.1.3) and the dominant
84 variable is the changes of temperature. Zhou et al. (2024) simulated the impact of the
85 Clean Air Action plan on ecosystem carbon assimilation and found that aerosol
86 reductions led to NPP increase of $20.1 \pm 10.9 \text{ TgCyr}^{-1}$ and the aerosol climatic effects on
87 NPP are twice those of the aerosol radiative effects. These studies indicated that there
88 were still large uncertainties in simulating the effects of aerosols on GPP (Liu et al.,
89 2021; Zhang et al., 2021b).

90 The uncertainties in aerosol-induced GPP changes could be induced by aerosol
91 direct and indirect effects and model sensitivities to climatic factors (defined as the
92 ecosystem climate sensitivity). Bellouin et al. (2020) reported that there were large
93 uncertainties in simulating aerosol radiative forcing. Additionally, many studies
94 demonstrated that the parameterization of vegetation photosynthesis within Earth
95 System Models (ESMs) also has large uncertainties (Hu et al., 2022; Gier et al., 2024).

96 Liu et al. (2021) showed that current LUE models have large bias in estimating the DFE.
97 However, it remains unclear whether the impact of aerosols on GPP simulated by
98 different ESMs is consistent and the dominant factors driving divergence among
99 different ESMs remain unclear. In this study, we used simulations with and without
100 anthropogenic aerosol emissions from the Coupled Model Intercomparison Project
101 Phase 6 (CMIP6). Our objectives of this study were: (1) to quantify the consistency
102 among CMIP6 models in estimating the impacts of aerosols on terrestrial GPP; (2) to
103 explore the contributors for inter-model differences. This multi-model assessment will
104 enhance our understanding of the interactions between anthropogenic aerosols, climate,
105 and terrestrial ecosystems.

106 **2. Data and method**

107 **2.1 CMIP6 simulations**

108 During the 1850-2014 period, the main anthropogenic aerosols simulated by
109 CMIP6 models are Sulfate, Organic Carbon (OC), and Black Carbon (BC) (Zhang et
110 al., 2022). The variations of anthropogenic aerosols are driven by anthropogenic and
111 biomass burning emissions. To investigate the effect of anthropogenic aerosols on
112 terrestrial GPP, we used the paired simulations from the Aerosol and Chemistry Model
113 Intercomparison Project (AerChemMIP), a CMIP6-endorsed activity (Collins et al.,
114 2017). We selected five Earth System Models (ESMs), including BCC-ESM1, IPSL-
115 CM6A-LR, NorESM2-LM, MPI-ESM-1-2-HAM, and UKESM1-0-LL. These models
116 have a diverse range of land surface components. Four of the five models considered
117 the differential effects of direct and diffuse radiation on canopy photosynthesis (Table
118 1). For each model, we compared the historical experiment against the hist-piAer
119 experiment from 1850 to 2014. The historical experiment is driven by all time-evolving
120 natural and anthropogenic forcings, while the hist-piAer experiment is run in parallel
121 with the historical experiment but fixes the anthropogenic aerosol emissions at pre-
122 industrial levels. This experimental design can be used to calculate the variations of
123 GPP induced by aerosols.

124 The monthly GPP, surface downwelling shortwave radiation (rsds), near-surface

125 air temperature (tas), top-of-atmosphere incident shortwave radiation (rsdt),
 126 precipitation (pr), total cloud cover percentage (clt), aerosol optical depth at 550nm
 127 (od550aer) from historical and hist-piAer experiments were used in this study. We also
 128 used the leaf area index (LAI) from historical and hist-piAer experiments to calculate
 129 the fraction of absorbed photosynthetically active radiation (PAR) by using Beer-
 130 Lambert law. The model simulations can be downloaded from Earth System Grid
 131 Federation (ESGF). Only NorESM2-LM and UKESM1-0-LL historical experiments
 132 provide diffuse radiation datasets. To illustrate the impact of DF on vegetation
 133 photosynthesis, we calculated the clearness index (CI, rsds/rsdt). Previous studies
 134 demonstrated that CI was strongly correlated with DF (Zhang et al., 2023c). We also
 135 show the scatter plots of DF against CI from these two models (Fig. S1). The results
 136 also indicate that there is a very high correlation between these two variables
 137 ($R^2=0.727$). All data were regridded to a resolution of $1.25^\circ \times 2.5^\circ$ (latitude by longitude).
 138 The impact of aerosols on GPP was isolated by comparing historical and hist-piAer
 139 scenarios (historical-hist-piAer).

140 Table 1. CMIP6 Earth system models (ESMs) used in this study. For each model, the land component
 141 model and whether the model accounts for the diffuse fertilization effect (DFE) on canopy photosynthesis
 142 or not are listed.

Model	Land component	DFE	References
IPSL-CM6A-LR	ORCHIDEE v2.0	NO	(Boucher et al., 2020)
MPI-ESM-1-2-HAM	JSBACH 3.20	YES	(Reick et al., 2021; Mauritsen et al., 2019)
NorESM2-LM	CLM	YES	(Lawrence et al., 2011; Lawrence et al., 2019)
BCC-ESM1	BCC_AVIM2	YES	(Li et al., 2019; Wu et al., 2020)

UKESM1-0-LL	JULES-ES-1.0	YES	(Sellar et al., 2019; Clark et al., 2011)
-------------	--------------	-----	--

143 **2.2 Observational data for model validation**

144 In this study, monthly eddy covariance flux measurements from FLUXNET were
145 used to assess the performance of GPP from CMIP6 ESMs. FLUXNET is a global
146 network of eddy covariance towers, which can provide measured data on energy, water,
147 and carbon dioxide exchanges between the biosphere and atmosphere (Pastorello et al.,
148 2020). In this study, we used datasets from FLUXNET2015, which has over 1,500 site-
149 years of measurements from 212 locations (Lasslop et al., 2010). We utilized data
150 records containing more than 80% of measured values and good quality gap-filled data
151 (NEE_VUT_REF_QC \geq 0.8) to ensure the quality of GPP. Fig. S2 shows monthly GPP
152 from five CMIP6 models (a-e) against FLUXNET site observations. The results reveal
153 a systematic underestimation of high GPP (slopes 0.406–0.632) and low coefficient of
154 determination ($R^2=0.305$ – 0.438) at the site scale. Additionally, we also used the
155 FLUXCOM-X products to evaluate the simulated GPP from CMIP6 ESMs.
156 FLUXCOM-X is the global terrestrial GPP and evapotranspiration (ET) products
157 derived from a newly data-driven scaling framework (X-BASE) (Nelson et al., 2024).
158 Nelson et al. (2024) demonstrated that the X-BASE dataset was significantly improved
159 compared to previous versions of FLUXCOM. The FLUXCOM-X products were also
160 regrided into 1.25° in latitude and 2.5° in longitude. Fig. S3 shows the performance of
161 monthly GPP from five CMIP6 ESMs (a-e) against the FLUXCOM-X GPP. The
162 coefficients of determination (R^2) for these models range from 0.517 to 0.678, with root
163 mean square errors (RMSEs) between 1.642 and 2.563 $\text{gC m}^{-2} \text{d}^{-1}$. The spatial
164 distribution of observed and simulated GPP from 2001 to 2014 were also shown in Fig.
165 S4.

166 **2.3 Attribution Framework of Inter-Model Spread**

167 The inter-model spread is attributed to discrepancies in simulated aerosol radiative
168 and climatic effects and the sensitivities of model to climatic factors. To quantify the
169 sources of uncertainty in aerosol-induced GPP changes, we developed an attribution

170 framework based on the method of Yu and Huang (2023). The framework is based on
 171 the biophysical principle that GPP is the product of photosynthetically active radiation
 172 (PAR), fraction of absorbed PAR (fPAR) and LUE. GPP can be calculated as follows:

$$173 \quad GPP = PAR * fPAR * LUE(tas, pr, CI) \quad (1)$$

174 where LUE is dependent on environmental conditions including tas, pr, and CI. To
 175 mathematically represent the aerosol-induced anomaly, a first-order Taylor expansion
 176 is applied to Equation 1:

$$177 \quad \delta GPP \approx \frac{\partial GPP}{\partial PAR} * \delta PAR + \frac{\partial GPP}{\partial fPAR} * \delta fPAR + \frac{\partial GPP}{\partial LUE} * \delta LUE \quad (2)$$

178 δGPP is the mean difference in GPP induced by anthropogenic aerosols during 1850-
 179 2014 and can be calculated by subtracting the GPP of hist-piAer from that of historical
 180 for each ESM. Equation 2 can be rewritten as

$$181 \quad \delta GPP \approx (fPAR * LUE) * \delta PAR + (PAR * LUE) * \delta fPAR + (PAR * fPAR) * \delta LUE \quad (3)$$

182 Bloomfield et al. (2022) showed that a generalized linear mixed-effects model could
 183 well represent the response of LUE to environmental factors. In addition, aerosol-
 184 induced changes in climatic variables are small. Therefore, the change in LUE (δLUE)
 185 can be approximated linearly:

$$187 \quad \delta LUE \approx \frac{\partial LUE}{\partial tas} \delta tas + \frac{\partial LUE}{\partial pr} \delta pr + \frac{\partial LUE}{\partial CI} \delta CI \quad (4)$$

188 Substituting Equation (4) into Equation (3) can get the full decomposition:

$$189 \quad \delta GPP \approx fPAR * LUE * \delta PAR + PAR * LUE * \delta fPAR + \frac{\partial LUE}{\partial tas} * fPAR * PAR * \delta tas + \frac{\partial LUE}{\partial pr} * fPAR * PAR * \delta pr + \frac{\partial LUE}{\partial CI} * fPAR * PAR * \delta CI \quad (5)$$

191 A multivariate regression model was constructed for specific plant functional type
 192 (PFT) and ESM to capture the impacts of climatic drivers and systematic model biases.

193 The regression equation for a specific model (m) is defined as:

$$194 \quad \delta GPP_m \approx \beta_{0,m} + \beta_{1,m} \delta PAR_m + \beta_{f,m} PAR_{clim} * \delta fPAR_m + \beta_{2,m} PAR_{clim} * \delta tas_m + \beta_{3,m} PAR_{clim} * \delta pr_m + \beta_{4,m} PAR_{clim} * \delta CI_m \quad (6)$$

196 Here, δGPP_m represents the aerosol-induced anomaly of GPP (Historical-Hist-piAer)
 197 from model m . PAR_{clim} is the climatological baseline PAR (0.45*rads). β_1 is the

198 product of fPAR and LUE, while β_f represents the baseline LUE. β_{2-4} represents the
 199 product of fPAR and the partial derivatives of LUE to climatic factors, while the
 200 intercept β_0 represents the systematic bias of the model. To address multicollinearity,
 201 standardized ridge regression was used for the specific PFT.

202 To quantify the inter-model divergence, we calculated the deviation of model m
 203 from the multi-model ensemble mean (mmm) by using the Equation 7.

$$204 \quad \Delta(\delta GPP) = \delta GPP_m - \delta GPP_{mmm} \quad (7)$$

205 By substituting the regression equations into Equation 7 and rearranging terms, we
 206 derived the final equation:

$$207 \quad \Delta(\delta GPP) = \underbrace{\sum_i \beta_{i,mmm} (X_{i,m} - X_{i,mmm})}_{\text{State contribution}} +$$

$$208 \quad \underbrace{\sum_i X_{i,m} (\beta_{i,m} - \beta_{i,mmm}) + (\beta_{f,m} X_{f,m} - \beta_{f,mmm} X_{f,m}) + (\beta_{0,m} - \beta_{0,mmm})}_{\text{Sensitivity contribution}} \quad (8)$$

209 where X_i represents the independent variables (including interaction terms). This
 210 equation decomposes the model spread into two components:

211 (1) State contribution: The divergence arising from differences in the simulated aerosol
 212 radiative and climatic effects (e.g., differences in simulated pr: $X_{i,m} - X_{i,mmm}$),
 213 weighted by the mean pr sensitivity ($\beta_{i,mmm}$).

214 (2) Sensitivity contribution: The divergence arising from ecosystem climate
 215 sensitivities across ESMs. This term represents the contributions from dynamic
 216 photosynthesis sensitivity differences ($\beta_{i,m} - \beta_{i,mmm}$), structural feedback divergence
 217 driven by LAI simulations ($\beta_{f,m} X_{f,m} - \beta_{f,mmm} X_{f,m}$) and the systematic bias
 218 differences ($\beta_{0,m} - \beta_{0,mmm}$).

219 **3. Results**

220 **3.1 The changes of global GPP induced by aerosols**

221 Fig. 1 shows the spatial patterns of aerosol-induced changes in GPP from five
 222 CMIP6 ESMs and their multi-model mean from 1850 to 2014. In the multi-model
 223 ensemble mean (Fig. 1a), aerosol loadings lead to a reduction in GPP ($0.0586 \text{ gC m}^{-2} \text{ d}^{-1}$),
 224 with 70.31% of global land areas experiencing decreased GPP. Notably, the Northern
 225 and Southern Hemispheres exhibit contrasting responses: most areas in the Northern

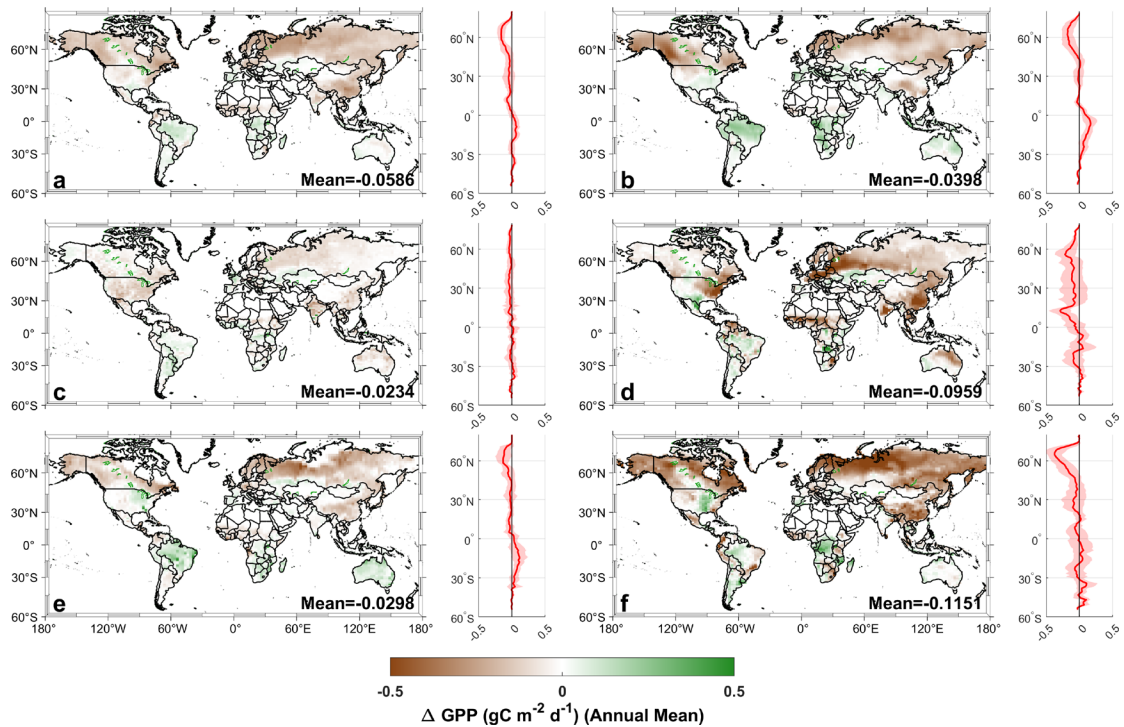
226 Hemisphere show decreased GPP, whereas some regions in the Southern Hemisphere
227 show modest increases. The results suggest that the changes of GPP induced by aerosols
228 in Northern and Southern Hemispheres are asymmetric. Large positive GPP anomalies
229 can be observed around 30°S, while a pronounced decline in GPP is shown around
230 70°N.

231 Among the individual models, BCC-ESM1 shows the general spatial pattern of the
232 multi-model ensemble mean but exhibits stronger regional variability. More areas show
233 positive GPP anomalies in BCC-ESM1 than in the multi-model ensemble mean over
234 the Northern Hemisphere. Weak aerosol effects are simulated by IPSL-CM6A-LR with
235 small changes in GPP. In contrast, MPI-ESM1-2-HAM model reveals large GPP
236 reductions across central and southern China, western Europe, and the eastern United
237 States. All these regions have relatively high aerosol emissions. NorESM2-LM shows
238 increased GPP in some areas of South America and decreased GPP over Europe.
239 UKESM1-0-LL shows increased GPP in the eastern United States, central Africa, and
240 parts of South America and decreased GPP across northern Europe and Asia.

241 In these models, decreased GPP can be found in northern mid-to-high latitudes and
242 eastern China. The result shows a robust signal of aerosol-induced suppression of
243 photosynthesis in these regions. Reduced GPP can be observed in 58.18%, 68.64%,
244 77.91%, 53.86%, and 72.94% of the global regions for BCC-ESM1, IPSL-CM6A-LR,
245 MPI-ESM-1-2-HAM, NorESM2-LM, and UKESM1-0-LL, respectively. The mean
246 aerosol-induced GPP change is -0.0398, -0.0234, -0.0959, -0.0298, and -0.1151 gC m⁻²
247 d⁻¹ from BCC-ESM1, IPSL-CM6A-LR, MPI-ESM-1-2-HAM, NorESM2-LM, and
248 UKESM1-0-LL, respectively. Although all models show the reduction in GPP, the
249 magnitude and spatial distribution of GPP changes vary greatly among models. These
250 discrepancies suggest the uncertainty in quantifying aerosol impacts on the terrestrial
251 carbon cycle in current ESMs.

252 In all four seasons, the CMIP6 models consistently show negative GPP anomalies
253 induced by aerosols. However, there are large differences in the magnitude and spatial
254 distribution (Fig. S5-8). In March–May, the multi-model ensemble mean reveals

255 widespread GPP reductions over the mid- and high-latitudes of the Northern
256 Hemisphere, particularly across East Asia and Europe. The differences among the
257 models are significant, with BCC-ESM1, MPI-ESM-1-2-HAM, and UKESM1-0-LL
258 simulating stronger reductions, while IPSL-CM6A-LR and NorESM2-LM show
259 weaker responses of GPP to aerosols. During the period of June–August, the variations
260 of GPP are greater and there are more regions showing positive anomalies. The
261 differences among models become more pronounced, especially in the low- and mid-
262 latitudes. For example, simulations from BCC-ESM1 and UKESM1-0-LL show that
263 the impacts of aerosols on GPP are positive in most regions of the United States and
264 Europe, whereas MPI-ESM-1-2-HAM reveals that the GPP anomalies are negative in
265 half of these regions. Meanwhile, the IPSL-CM6A-LR model simulation indicates that
266 the changes of GPP are negative over the United States. In September–November, the
267 negative anomalies are also shown but weaker than those during the period of June–
268 August. Over Australia, the aerosol effects on GPP are positive from BCC-ESM1 and
269 NorESM2-LM, but negative from IPSL-CM6A-LR and MPI-ESM-1-2-HAM. In
270 December–February, aerosols consistently exhibit a small negative effect on GPP in the
271 Northern Hemisphere, whereas model simulations show large discrepancies in the
272 Southern Hemisphere. In all, these results demonstrate that aerosols generally suppress
273 global GPP, but with significant differences in the amplitude and spatial distribution
274 among models.

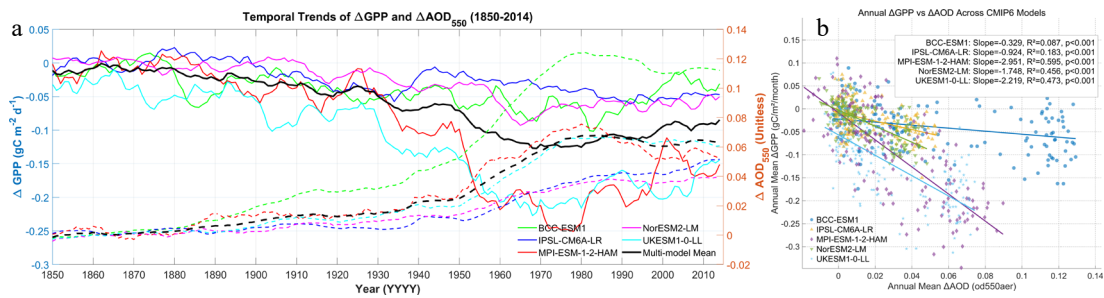


275

276 Figure 1. The spatial pattern of changes in ecosystem GPP ($\text{gC}/(\text{m}^2\text{d})$) induced by aerosols from CMIP6
 277 models (a. multi-model mean, b. BCC-ESM1, c. IPSL-CM6A-LR, d. MPI-ESM-1-2-HAM, e.
 278 NorESM2-LM, f. UKESM1-0-LL).

279 Fig. 2a shows the time series of the ten-year average changes of GPP induced by
 280 aerosols and AOD variations from 1850 to 2014. The results show that global GPP and
 281 AOD have experienced large variations. The aerosol-induced GPP changes show a
 282 decreasing trend from 1850 to the mid-20th century, with a marked shift around the
 283 1950s. This reduction was induced by the increasing aerosol emissions. From 1850 to
 284 1890, some models show a positive impact of aerosols on GPP. However, the increment
 285 in ΔAOD during this period is negligible across all models. This indicates that
 286 anthropogenic aerosols have little impacts on the change of GPP from 1850 to 1890.
 287 The absence of a consistent directional GPP response suggests that these variations
 288 might be related to the internal climate variability noise. After 1980, an increase in GPP
 289 can be observed. This aligns with the decreasing aerosol loadings. There are notable
 290 differences between the models in the magnitude and timing of GPP and AOD changes.
 291 MPI-ESM-1-2-HAM and UKESM1-0-LL exhibit a larger variation of GPP compared
 292 to the other models. Fig. 2b shows the scatter plots of the annual mean of GPP changes

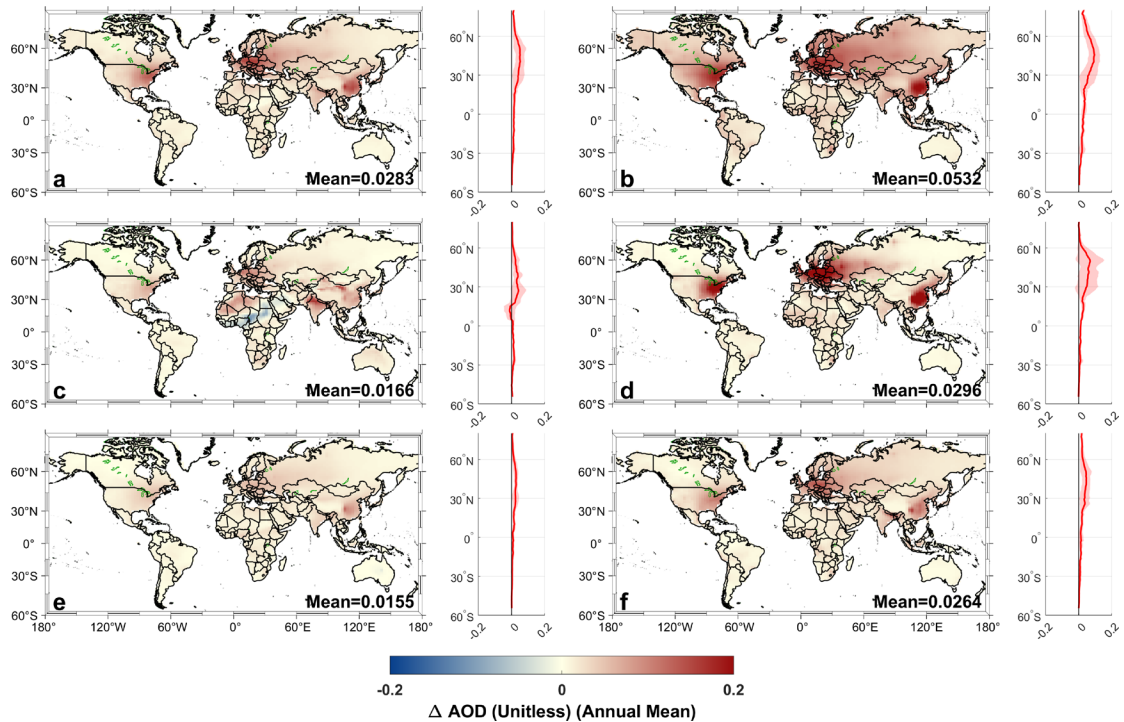
293 induced by aerosols against the AOD variations. Aerosol-induced changes in GPP are
 294 significantly related to the AOD ($p < 0.001$). However, the sensitivities of GPP to aerosol
 295 loadings are different among models. These discrepancies highlight the uncertainty in
 296 simulating atmospheric aerosol loadings and the impact of aerosols on global
 297 productivity.



298
 299 Figure 2. (a) Time series of aerosol-induced GPP changes (solid lines) and AOD variations (dashed
 300 lines) from 1850 to 2014 with a ten-years moving window; (b) The scatter plots of annual mean of
 301 GPP changes induced by aerosols against the AOD variations.

302 3.2 Changes of aerosols and meteorological factors

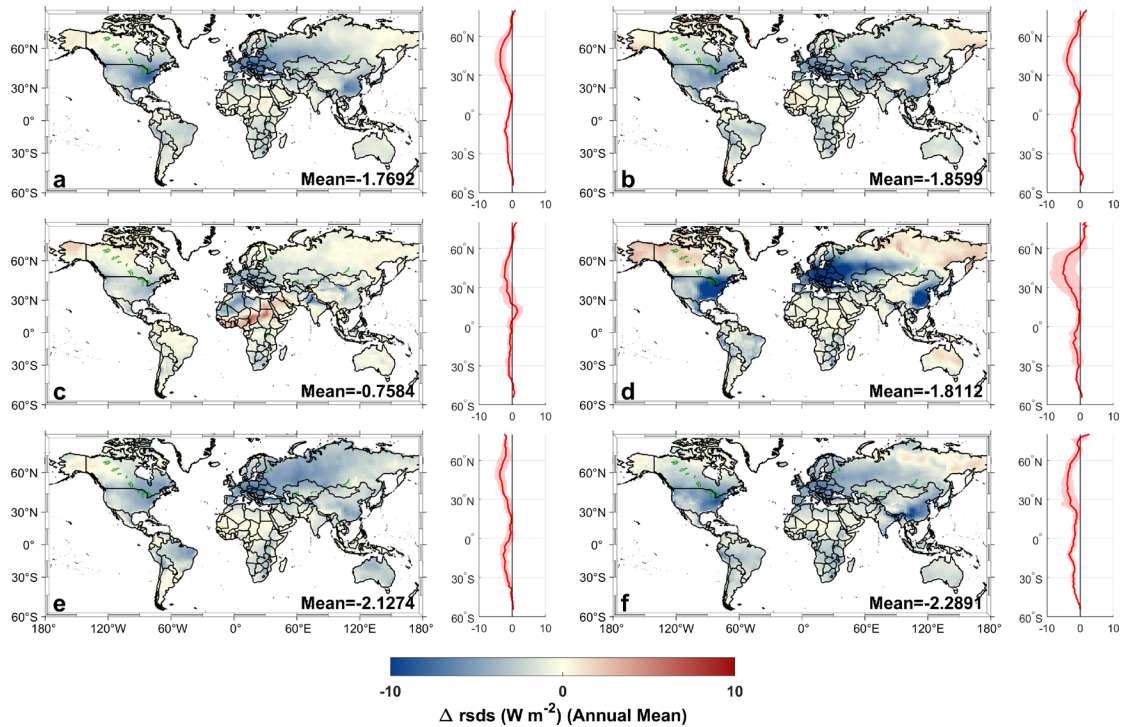
303 Analysis of AOD differences at 550 nm (od550aer) between historical and hist-
 304 piAer experiments reveals significant discrepancies among CMIP6 ESMs (Fig. 3). The
 305 multi-model ensemble mean differences in AOD (Fig. 3a) show significant increase in
 306 AOD across northern mid-latitudes, especially in major industrial regions including
 307 North America, Europe, and East Asia. In contrast, IPSL-CM6A-LR (Fig. 3c) shows
 308 decreased AOD in some regions. MPI-ESM-1-2-HAM (Fig. 3d) and UKESM1-0-LL
 309 (Fig. 3f) show high aerosol loadings in industrialized regions of North America and
 310 Eurasia. NorESM2-LM (Fig. 3e) shows a relatively modest aerosol increase. The
 311 spatial distribution of AOD reveals substantial inter-model discrepancies in simulating
 312 the global aerosol loadings.



313

314 Figure 3. The spatial pattern of mean differences of aerosol optical depth (AOD) at 550nm (od550aer)
 315 between historical and hist-piAer experiments over the period 1850–2014 (a. multi-model mean, b. BCC-
 316 ESM1, c. IPSL-CM6A-LR, d. MPI-ESM-1-2-HAM, e. NorESM2-LM, f. UKESM1-0-LL).

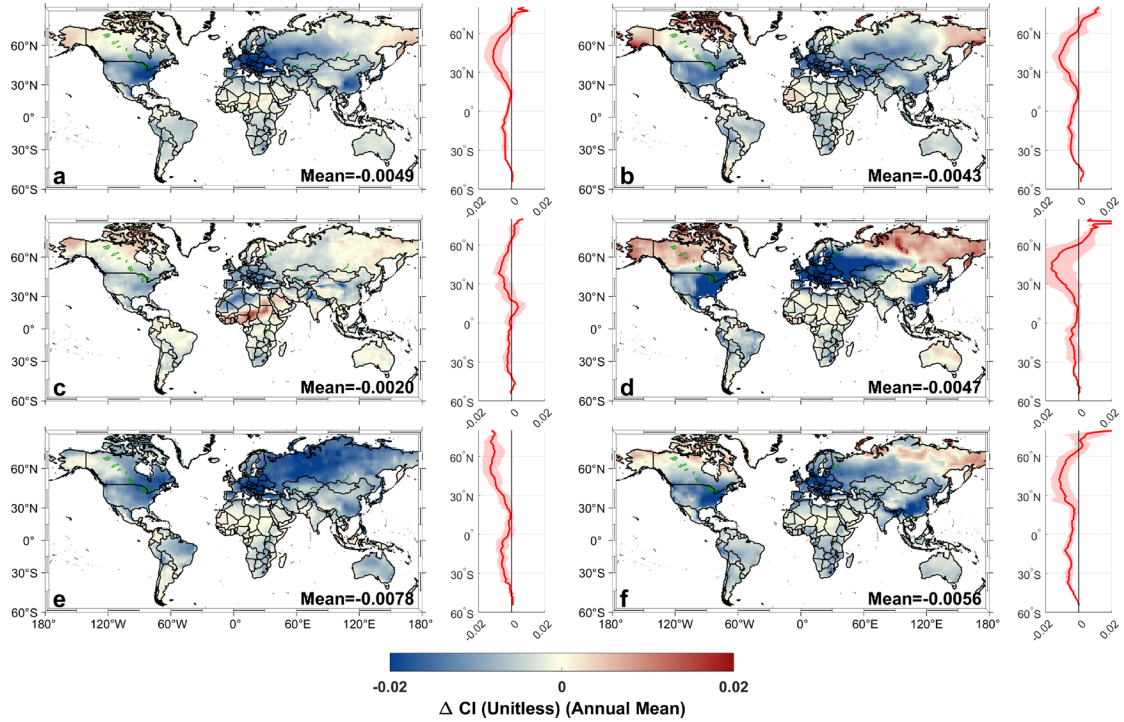
317 Analysis of mean differences in rsds between historical and hist-piAer scenarios
 318 further demonstrates pronounced inter-model variability (Fig. 4). The multi-model
 319 ensemble mean differences in rsds (Fig. 4a) show reduction in most of the regions,
 320 especially in northern mid-latitudes. Models such as BCC-ESM1 (Fig. 4b) and
 321 UKESM1-0-LL (Fig. 4f) show similar spatial distribution of variations in rsds. Among
 322 all models, MPI-ESM-1-2-HAM (Fig. 4d) has the largest area where rsds increases.
 323 NorESM2-LM (Fig. 4e) show widespread decreases. IPSL-CM6A-LR (Fig. 4c)
 324 presents a more complex spatial distribution, highlighting reductions in shortwave
 325 radiation over parts of Eurasia and Africa but also notable regional increases. This is
 326 consistent with the spatial distribution of AOD. The result shows that there are large
 327 differences among ESMs in simulating radiation.



328

329 Figure 4. The spatial distribution of mean differences of shortwave radiation (rsds, W/m^2) between
 330 historical and hist-piAer experiments from 1850 to 2014 (a. multi-model mean, b. BCC-ESM1, c. IPSL-
 331 CM6A-LR, d. MPI-ESM-1-2-HAM, e. NorESM2-LM, f. UKESM1-0-LL).

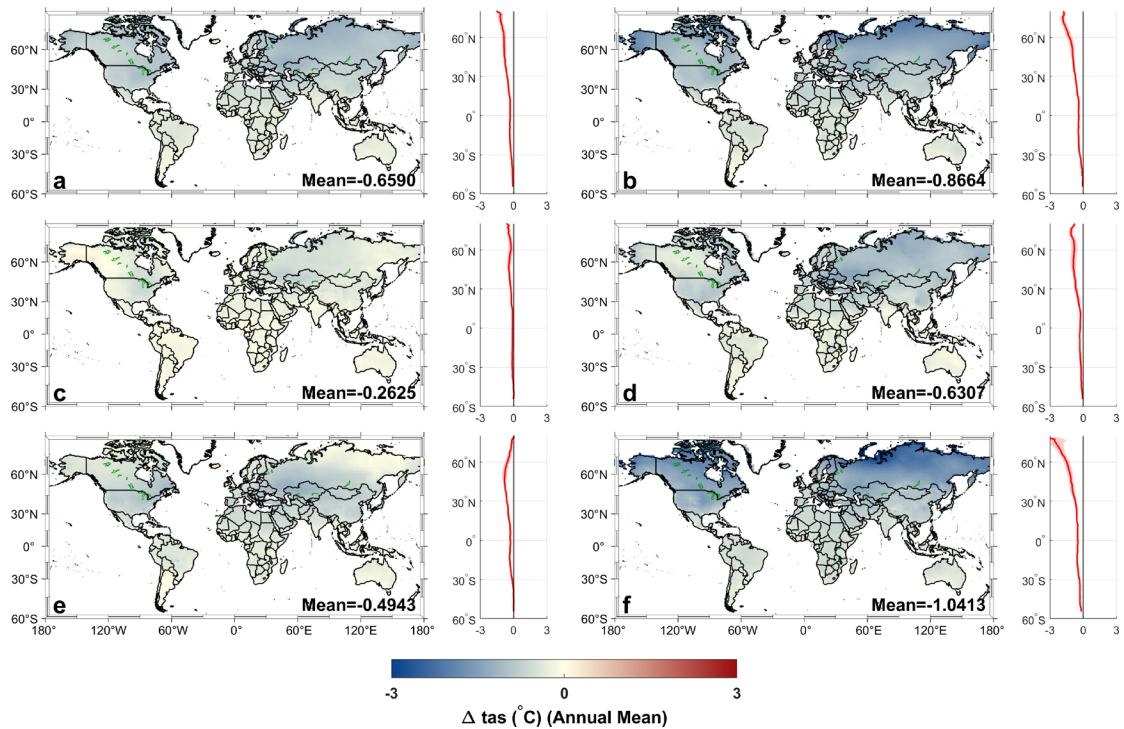
332 The spatial distribution of mean differences in the CI between historical and hist-
 333 piAer scenarios is consistent with that of rsds. BCC-ESM1 (Fig. 5b) and UKESM1-0-
 334 LL (Fig. 5f) show the decreases in CI in most regions. The CI decreases significantly
 335 in northern mid-latitude regions with the high aerosol loadings. In the NorESM2-LM
 336 (Fig. 5e), CI shows a decreasing trend in almost all regions. IPSL-CM6A-LR (Fig. 5c)
 337 reveals heterogeneous changes, with localized areas showing increased CI amidst
 338 predominant decreases. The result also shows large discrepancies in simulating the
 339 variations of CI induced by the aerosols.



340

341 Figure 5. The spatial pattern of mean differences of clearness index (CI) between historical and hist-
 342 piAer experiments from 1850 to 2014 (a. multi-model mean, b. BCC-ESM1, c. IPSL-CM6A-LR, d. MPI-
 343 ESM-1-2-HAM, e. NorESM2-LM, f. UKESM1-0-LL).

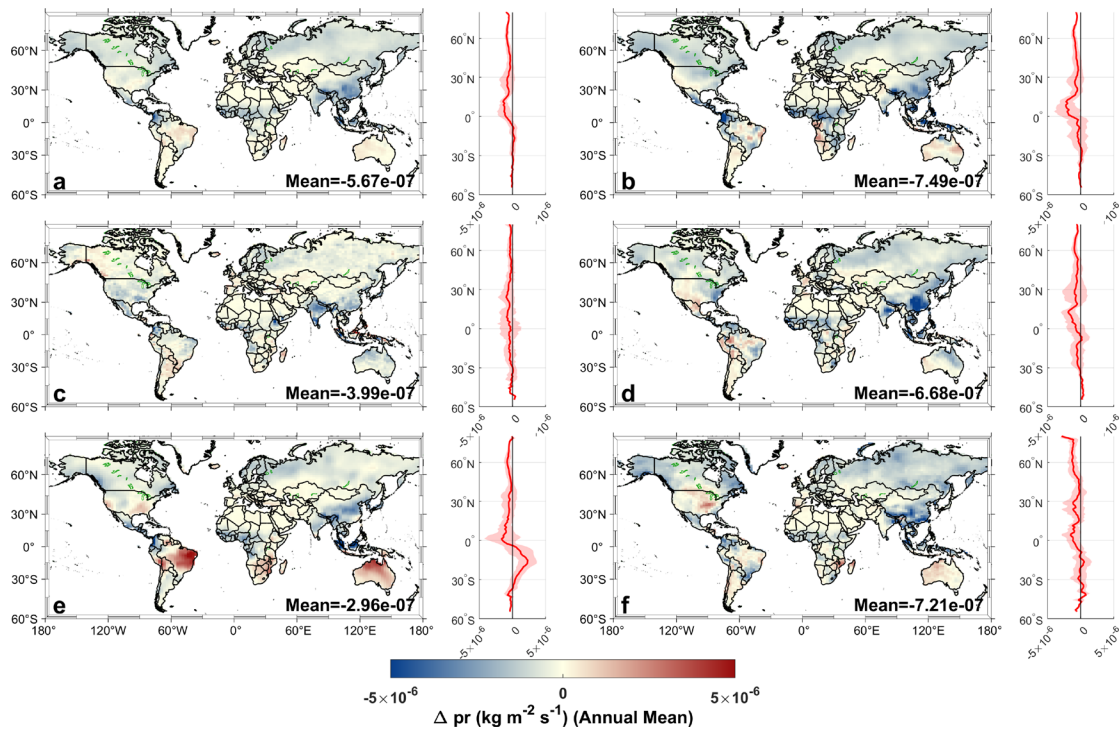
344 The spatial distribution of mean differences in tas between historical and hist-piAer
 345 scenarios reveals consistent cooling trends in response to increased aerosol loadings
 346 across these models in CMIP6 (Fig. 6). The multi-model ensemble mean differences of
 347 tas (Fig. 6a) shows that aerosols can induce the decrease in tas. BCC-ESM1 (Fig. 6b),
 348 MPI-ESM-1-2-HAM (Fig. 6d), and UKESM1-0-LL (Fig. 6f) prominently show
 349 widespread cooling in the Northern Hemisphere. The tas in high-latitude areas of the
 350 Northern Hemisphere decreases more than that in mid- and low-latitude regions. The
 351 temperature in the Southern Hemisphere is less affected than that in the Northern
 352 Hemisphere. NorESM2-LM (Fig. 6e) and IPSL-CM6A-LR (Fig. 6c) also exhibit
 353 decreased tas, but with weaker magnitude.



354

355 Figure 6. The spatial pattern of mean differences of near-surface air temperature (tas, °C) between
 356 historical and hist-piAer experiments from 1850 to 2014 (a. multi-model mean, b. BCC-ESM1, c. IPSL-
 357 CM6A-LR, d. MPI-ESM-1-2-HAM, e. NorESM2-LM, f. UKESM1-0-LL).

358 Analysis of mean differences in pr between historical and hist-piAer scenarios
 359 reveals that there are also large differences in simulating the impact of aerosols on pr
 360 across CMIP6 models (Fig. 7). The multi-model ensemble mean differences of pr show
 361 that aerosols induce a reduction in pr in most regions (Fig. 7a). BCC-ESM1 (Fig. 7b)
 362 shows modest decrease in pr across mid-latitudes and tropical regions. In contrast,
 363 IPSL-CM6A-LR (Fig. 7c), MPI-ESM-1-2-HAM (Fig. 7d), NorESM2-LM (Fig. 7e),
 364 and UKESM1-0-LL (Fig. 7f) show complex spatial distribution of pr changes, with
 365 both pronounced regional increases and decreases. The response of pr to aerosols
 366 suggests that there are some uncertainties in aerosol-cloud interactions. This may also
 367 induce the uncertainties in simulating regional hydrological cycles.



368

369 Figure 7. The spatial pattern of mean differences of precipitation (pr, kg/(m²s)) between historical and
 370 hist-piAer experiments from 1850 to 2014 (a. multi-model mean, b. BCC-ESM1, c. IPSL-CM6A-LR, d.
 371 MPI-ESM-1-2-HAM, e. NorESM2-LM, f. UKESM1-0-LL).

372 3.3 Attribution of Inter-Model Spread in aerosol-induced GPP changes

373 We applied the attribution framework to quantify the drivers of inter-model spread
 374 in aerosol-induced GPP anomalies. The framework decomposes the total spread into
 375 contributions from aerosol radiative and climatic effects (“state”) and ecosystem
 376 climate sensitivities (“sensitivity”). The framework captures the variability of aerosol-
 377 induced GPP changes for all ESMs, with the R² ranging from 0.514 to 0.788 (Fig. 8c,
 378 red line). The framework can explain more than 50% of GPP changes. We also showed
 379 the performance of the attribution framework across ESMs per PFT (Table S1). The
 380 coefficient of determination (R²) exceeds 0.6 across different ESMs and PFTs. These
 381 results suggest that the framework can be used for analyzing the contribution of “state”
 382 and “sensitivity”.

383 The decomposition of total spread reveals the dominant driver (Fig. 8c, bars). The
 384 GPP anomalies in NorESM2-LM are dominated by state contributions (80.5%). This
 385 indicates that the aerosol radiative and climatic effects simulated by this model have a

386 large difference with the ensemble mean. In contrast, the main driver of BCC-ESM1,
387 IPSL-CM6A-LR, MPI-ESM-1-2-HAM, and UKESM1-0-LL is the sensitivity
388 contributions, accounting for 143.6%, 165.2%, -71.8%, and -138.2%, respectively. This
389 implies a divergence in model ecological parameterization. Four of five models show
390 that the sensitivity contribution is higher than the state contribution in the inter-model
391 spread. The inter-model discrepancies in aerosol-induced GPP changes are driven by
392 the parameterization of canopy photosynthesis in the ESMs.

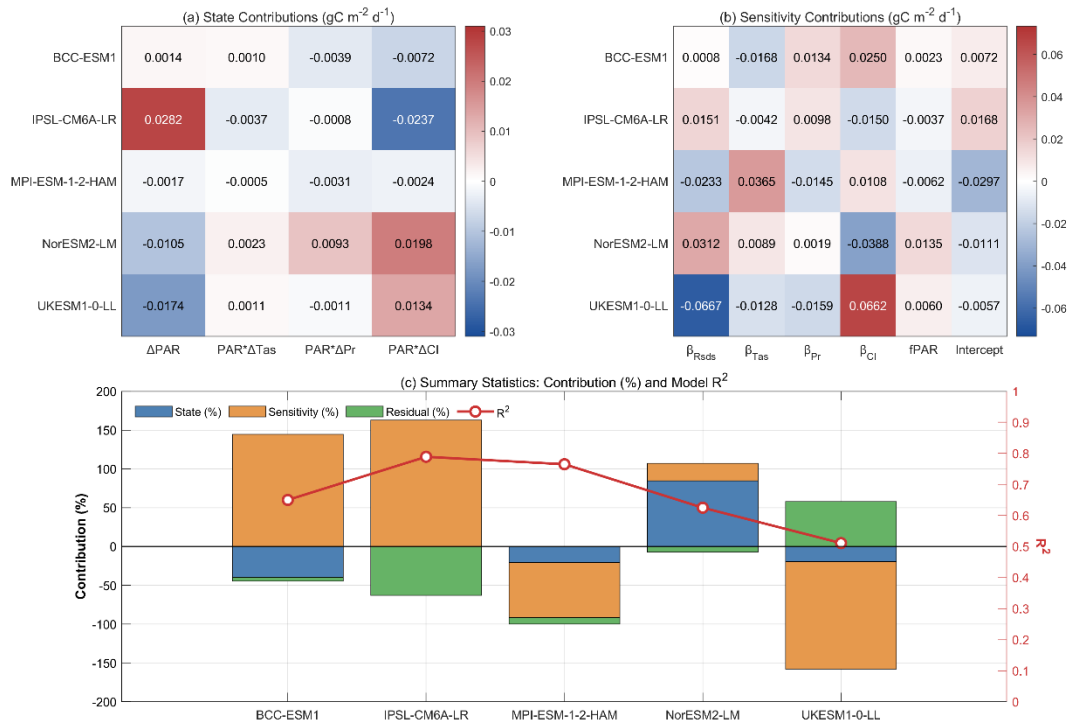
393 Fig. 8a shows the contribution of discrepancies in simulated aerosol radiative and
394 climatic effects across models. IPSL-CM6A-LR shows that radiation anomalies have a
395 large positive contribution ($0.0282 \text{ gC m}^{-2}\text{d}^{-1}$). This indicates that this model simulates
396 a weaker aerosol dimming effect than other models (Fig. 4c). This is the primary driver
397 for positive GPP anomalies of IPSL-CM6A-LR. For UKESM1-0-LL, radiation shows
398 a strong negative contribution ($-0.0174 \text{ gC m}^{-2}\text{d}^{-1}$). This means that the aerosol-induced
399 dimming effect simulated by UKESM1-0-LL is stronger than those of other models
400 (Fig. 4f). For NorESM2-LM, the interaction between PAR and CI plays a prominent
401 role ($0.0198 \text{ gC m}^{-2}\text{d}^{-1}$). The interaction between PAR and CI also plays an important
402 role in IPSL-CM6A-LR, but with a negative effect ($-0.0237 \text{ gC m}^{-2}\text{d}^{-1}$).

403 Fig. 8b shows the contribution of ecosystem climate sensitivities to the inter-model
404 spread in GPP anomalies. The parameterization of model canopy photosynthesis will
405 induce the divergence in ecosystem climate sensitivities to temperature, precipitation,
406 and radiation. Large difference in the response of photosynthesis to radiation can be
407 observed. This indicates that the assumption of canopy radiative transfer in the ESMs
408 introduces some differences in the response of photosynthesis to radiation. β_{PAR} and
409 β_{CI} represent the sensitivity of vegetation photosynthesis to light quantity and light
410 quality (light composition and spectral distribution), respectively. The sensitivities of
411 photosynthesis to CI (β_{CI}) from BCC-ESM1 ($0.0250 \text{ gC m}^{-2}\text{d}^{-1}$) and UKESM1-0-LL
412 ($0.0662 \text{ gC m}^{-2}\text{d}^{-1}$) show positive contributions to GPP anomalies. This suggests that
413 these models simulate a stronger diffuse fertilization effect than the multi-model
414 ensemble mean. For UKESM1-0-LL, the diffuse fertilization effect partially reduces by

415 the covaried decreased PAR (β_{PAR} : $-0.0667 \text{ gC m}^{-2}\text{d}^{-1}$). IPSL-CM6A-LR shows the
416 opposite pattern with a positive contribution from PAR sensitivity ($0.0151 \text{ gC m}^{-2}\text{d}^{-1}$)
417 and a negative contribution from CI sensitivity ($-0.0150 \text{ gC m}^{-2}\text{d}^{-1}$). This indicates that
418 the assumption of canopy radiative transfer in this model is insensitive to the variations
419 of light quality. The sensitivity of photosynthesis to temperature reveals the different
420 thermal adaptation strategies used in the ESMs. MPI-ESM-1-2-HAM shows the highest
421 positive contribution of temperature (β_{tas} : $0.0365 \text{ gC m}^{-2}\text{d}^{-1}$). This suggests that this
422 model has a larger GPP gain under aerosol-induced cooling compared to the multi-
423 model ensemble mean. Conversely, BCC-ESM1 shows a negative contribution of
424 temperature sensitivity ($-0.0168 \text{ gC m}^{-2}\text{d}^{-1}$). This indicates that the photosynthesis in
425 the model gains less than other ESMs. The sensitivity of photosynthesis to precipitation
426 (β_{pr}) links to the soil hydrology schemes and the response of stomatal conductance to
427 water stress. The contribution of precipitation sensitivity to GPP anomalies is generally
428 smaller than that of other environmental factors across most models. This suggests that
429 the response of ESMs to precipitation is relatively consistent. BCC-ESM1 and IPSL-
430 CM6A-LR show a moderate positive contribution of precipitation sensitivity (0.0134
431 and $0.0098 \text{ gC m}^{-2}\text{d}^{-1}$), while other three models show a small negative contribution.
432 We also calculate the intercept (residual) term, which can represent the systematic
433 deviation in baseline productivity from the ensemble mean. For MPI-ESM-1-2-HAM
434 and NorESM2-LM, the baseline bias shows large negative contributions (-0.0297 and
435 $-0.0111 \text{ gC m}^{-2}\text{d}^{-1}$, respectively). This demonstrates that the offsets in base-state
436 parameterizations (e.g., lower V_{cmax} compared to the MMM) is also a major source of
437 uncertainty in simulating the effect of aerosols on plant productivity.

438 To analyze the spatial distribution of dominant driver governing the inter-model
439 spread in aerosol-induced GPP anomalies, we showed the state and sensitivity
440 contributions onto the global spatial grid (Figure S9). The results from spatial
441 distribution further confirmed that the sensitivity contribution is the primary driver of
442 GPP anomalies induced by aerosols. The contribution of ecosystem climate sensitivities
443 ranges from 57.5% in NorESM2-LM to 78.7% in UKESM1-0-LL. Although the

444 primary driver for each model is the sensitivity contribution, the spatial maps reveal
 445 significant inter-model divergence in the directionality of the sensitivities. MPI-ESM-
 446 1-2-HAM and UKESM1-0-LL show widespread negative sensitivity contributions in
 447 most regions, while BCC-ESM1, MPI-ESM-1-2-HAM, and UKESM1-0-LL exhibit
 448 widespread negative state contributions in most regions.



449
 450 Figure 8. Decomposition of drivers governing the inter-model spread in aerosol-induced GPP anomalies.
 451 Contributions (gC m⁻²d⁻¹) arising from differences in (a) aerosol radiative and climatic effects (State;
 452 including ΔPAR and interaction terms) and (b) ecosystem climate sensitivities (Sensitivity; including
 453 dynamic $\Delta\beta$ and residual). (c) Aggregated relative contributions (bars) and coefficient of determination
 454 (R^2 , line). Components: State (blue), Sensitivity (orange), Residual (green).

455 4. Discussion

456 4.1 Divergent aerosol impacts on terrestrial GPP in CMIP6 models

457 This study revealed significant inter-model divergence among CMIP6 ESMs in
 458 simulating the effect of aerosols on terrestrial GPP. In this study, we showed that the
 459 anthropogenic aerosols decreased the terrestrial GPP in all ESMs from 1850 to 2014
 460 and the decreased GPP increased with the AOD. Zhang et al. (2023a) and Zhou et al.
 461 (2024) also showed that the anthropogenic aerosols caused a reduction of terrestrial

462 carbon sink. This is generally consistent with the results in this study. However, Zhang
463 et al. (2021a) reported that anthropogenic aerosols increased terrestrial carbon sink by
464 22.6 PgC using ORCHIDEE_DF land components and IPSL-CM6A-LR climate and
465 aerosol forcing data. This bias might be induced through two pathways. First, AOD
466 from IPSL-CM6A-LR is lower than that from other models. Second, a new
467 development of ORCHIDEE trunk (ORCHIDEE_DF) with two-stream canopy light
468 transmission model was used, which can better capture the diffuse radiation fertilization
469 effect than the original IPSL-CM6A-LR model (Zhang et al., 2020).

470 **4.2 Ecosystem climate sensitivities of ESMs in CMIP6**

471 Our attribution framework reveals that the substantial inter-model spread in
472 aerosol-induced GPP anomalies is not merely caused by the divergent aerosol radiative
473 and climatic effects, but is also governed by the terrestrial ecosystem climate
474 sensitivities. This finding challenges the traditional view of improving the simulation
475 of aerosol radiative and climatic effects alone and suggests that ecosystem climate
476 sensitivities of ESMs are also a dominant source of uncertainties in simulating aerosol-
477 induced GPP changes. Inter-model differences in ecosystem climate sensitivities
478 primarily came from the radiation and temperature sensitivities of photosynthesis in the
479 ESMs.

480 A critical source of divergence lies in the representation of canopy radiative transfer,
481 specifically the response to light quality. Compared to the MMM, UKESM1-0-LL
482 shows strong positive anomalies in the sensitivity to diffuse radiation. The sensitivity
483 coefficients for CI from UKESM1-0-LL are lowest in 8 out of 11 PFTs (Table S6). This
484 behavior is controlled by the land component (JULES). The model uses a multi-layer
485 canopy scheme with explicit light interception calculations for sunlit and shaded leaves
486 at each depth (Sellar et al., 2019; Clark et al., 2011). This canopy radiative transfer
487 model allows the diffuse radiation to reach the deeper canopy and can capture the DFE.
488 The IPSL-CM6A-LR shows the lowest DFE among all five models, because the model
489 uses a standard “big leaf” approach and does not consider the DFE (Cheruy et al., 2020;
490 Zhang et al., 2020). Table S6 shows that sensitivity coefficients for CI from IPSL-

491 CM6A-LR approach zero across almost all PFTs. NorESM2-LM (CLM5) integrates a
492 revised two-stream approximation with the Medlyn stomatal conductance model
493 (Lawrence et al., 2019). This combination also can capture the DFE ($\beta_{CI} < 0$ in major
494 PFTs). However, this model shows lower DFE than other models and this might be
495 induced by the nutrient limitation.

496 Most land components of ESMs use the traditional Farquhar-Berry-Collatz
497 framework for simulating photosynthesis (Arora, 2003; Clark et al., 2011; Reick et al.,
498 2021; Boucher et al., 2020). However, our results showed that there were large
499 differences in the temperature sensitivities (β_{tas}) and structural feedbacks (fPAR)
500 across different PFTs (Table S3 and S4). This is because there are large differences in
501 how they consider the influence of temperature on GPP. The impact of temperature on
502 photosynthesis can be divided into three parts, including chemical limits, adaptation to
503 heat, and phenology. For the level of immediate chemical reactions, the models have
504 some differences in estimating the response of V_{cmax} and J_{max} to temperature. MPI-
505 ESM-1-2-HAM (JSBACH 3.2) adopts a strict physical chemistry approach. The
506 method uses the Arrhenius equation and a specific inhibition function to calculate the
507 impact of temperature on key rates (Reick et al., 2021). When the temperature is higher
508 than about 55°C, the photosynthetic rates will be zero. In contrast, UKESM1-0-LL
509 (JULES) adopts a formula based on Q_{10} factors (Clark et al., 2011). These divergent
510 responses are captured by the β_{Tas} values (Table S4). At the level of adaptation to heat,
511 NorESM2 (CLM5) introduces a mechanism for thermal acclimation based on the
512 LUNA module (Lawrence et al., 2019). BCC-ESM1 and IPSL-CM6A-LR use a
513 traditional method, which assumes that the response of plants to temperature is fixed
514 (Boucher et al., 2020; Li et al., 2019). CLM5 can adjust the nitrogen-use efficiency
515 based on past environmental conditions. Therefore, the photosynthetic capacity (V_{cmax25})
516 in the model also changes dynamically. This will improve the accuracy of GPP in the
517 area with big seasonal changes and the photosynthesis in the model might be more
518 sensitive to warming than the model used traditional method. The plant phenology in
519 BCC-ESM1 (BCC_AVIM2.0) is controlled by temperature (Li et al., 2019). The model

520 adopts a method based on accumulated heat to determine when leaves grow. This is
521 different from JSBACH, which uses chill days to break dormancy (Reick et al., 2021).
522 Therefore, BCC-ESM1 uses heat to support growth, while JSBACH focuses on the end
523 of cold days. This difference will lead to some divergences in predicting when the
524 growing season starts, especially in cold regions. Our results are fully consistent with
525 the theory. Table S3 showed that the structural feedback of BCC-ESM1 is generally the
526 highest among all ESMs across almost all PFTs. This suggests that heat-accumulation
527 phenology scheme of BCC-ESM1 makes the vegetation phenology more sensitive to
528 temperature changes induced by aerosols. In summary, these models use different
529 methods to estimate the impact of temperature on photosynthesis and this will lead to
530 the different response of GPP to temperature.

531 **4.3 Limitations and implications for future projections**

532 Validation against FLUXNET observations reveals a systemic underestimation of
533 GPP across all five models (Figure S2). However, this underestimation is largely
534 attributed to the scale mismatch between ground-based eddy covariance measurements
535 and model grid pixels. Comparisons of CMIP6 ESMs against the FLUXCOM-X did
536 not show this underestimation (Figure S3). This indicates that ESMs can capture the
537 global GPP magnitudes. Our attribution framework incorporated a systematic bias term
538 to account for the bias of GPP. In addition, our framework was developed to investigate
539 the sources of inter-model spread, rather than to evaluate the accuracy of model
540 simulations. This also mitigates the direct impact of GPP bias on our analysis.

541 Although the attribution framework in this study can capture more than 50% of
542 inter-model GPP spreads, there are still large remaining unexplained variations. First,
543 the framework omits higher-order non-linear climate interactions. For example,
544 heatwaves accompanied by concurrent precipitation deficits exert an exponentially
545 influence on VPD and vegetation stomatal conductance (Wang et al., 2025). Second,
546 we utilized precipitation as the primary hydrological driver. However, precipitation
547 might not adequately reflect the actual water stress on vegetation photosynthesis in
548 some regions (Song et al., 2022). Third, the unexplained inter-model spread is highly

549 related to unaccounted biogeochemical constraints, particularly the nutrition limitations
550 in the model. Furthermore, it is impossible to fully disentangle internal climate
551 variability by using single ensemble member per model. This limitation mainly occurs
552 during the early industrial period, when the AOD changes are small and is comparable
553 in magnitude to the internal climate variability induced noise in the GPP difference
554 between historical and hist-piAer simulations.

555 In this study, our framework identified structural and physiological mechanisms
556 driving the inter-model spread in simulating the response of photosynthesis to aerosols.
557 This also highlights the pathways for future model evaluation and reducing the inter-
558 model spread. First, canopy radiative transfer module should be evaluated to make sure
559 that the model can capture the impacts of diffuse and direct radiation accurately. Some
560 parameters that affect canopy radiation transfer module should be evaluated and
561 incorporated into the model. For example, Li et al. (2023) reported that the light
562 environment within canopy was affected by the clumping index. However, many ESMs
563 do not incorporate the clumping index and this will induce some uncertainties in
564 simulating the canopy light environment (Fang, 2021). Second, the responses of
565 photosynthesis to soil moisture and air temperature require rigorous validation (Gabele
566 et al., 2025). Although some models have incorporated the acclimation of
567 photosynthesis via various approaches, most of the approaches were not sufficient to
568 capture the non-linear impact of air temperature and precipitation on photosynthesis.
569 Eco-evolutionary optimality (EEO) theories offer an opportunity to re-evaluate and
570 constrain the underlying physiological responses (Ren et al., 2025). Using these
571 observation-supported theories to evaluate the ESMs is the key to reducing the
572 uncertainties in simulating the response of photosynthesis to temperature and
573 precipitation.

574 **5. Summary**

575 Anthropogenic aerosol loadings have increased significantly since 1850. The
576 increased aerosols can significantly affect the terrestrial carbon cycle through reducing
577 the total shortwave radiation, increasing the diffuse radiation fraction, and altering the

578 temperature and precipitation. Many models were developed for simulating the effects
579 of aerosols on regional terrestrial carbon cycle. However, divergence among models in
580 simulating the effects of aerosols on gross primary production (GPP) still need further
581 investigation. In this study, we investigated the differences in simulating the aerosol-
582 induced GPP changes among the models and the driving factors using five Earth System
583 Models (ESMs) from CMIP6, including BCC-ESM1, IPSL-CM6A-LR, MPI-ESM-1-
584 2-HAM, NorESM2-LM, and UKESM1-0-LL. Our results indicated that all five models
585 simulated a reduction in global GPP. However, there are large uncertainties in the
586 magnitude and spatial distribution of these changes. Our results showed that inter-
587 model spread was mainly caused by terrestrial ecosystem climate sensitivities, rather
588 than atmospheric aerosol radiative and climatic effects in ESMs. Specifically, the
589 divergence was mainly induced by the different assumptions of canopy radiative
590 transfer and thermal acclimation. Our findings indicated that refining atmospheric
591 aerosol optical properties alone was insufficient to reduce inter-model spread in
592 simulating aerosol-induced GPP changes. Future efforts should be used to improve the
593 response of photosynthesis to climatic factors.

594 **Code and data availability**

595 All model outputs from the Coupled Model Intercomparison Project Phase 6 (CMIP6)
596 (Earth System Grid Foundation, 2024) used in this paper are publicly available at
597 <https://aims2.llnl.gov/search/cmip6/> (Eyring et al., 2016). FLUXNET data are obtained
598 from Pastorello et al. (2020). FLUXCOM-X data can be accessed from the ICOS
599 Carbon Portal (Nelson et al., 2023). The post-processing scripts are available at
600 <https://doi.org/10.5281/zenodo.18396248> (Zhang, 2026).

601 **Author contributions**

602 Zhaoyang Zhang: Formal analysis; visualization; investigation; writing – original draft.
603 Meng Fan: Methodology; writing – review and editing. Minghui Tao, and Yunhui Tan:
604 Investigation. Quan Wang: writing – review and editing.

605 **Competing interests**

606 The contact author has declared that none of the authors has any competing interests.

607 **Acknowledgements**

608 We acknowledge the World Climate Research Programme's Working Group on
609 Coupled Modelling, which is responsible for CMIP.

610 **Financial support**

611 This work was supported by the National Natural Science Foundation of China (Grant
612 No. 42171366, 42375132, and 41801258).

613 **References**

614 Anav, A., Friedlingstein, P., Beer, C., Ciais, P., Harper, A., Jones, C., Murray-Tortarolo, G., Papale, D.,
615 Parazoo, N. C., Peylin, P., Piao, S. L., Sitch, S., Viovy, N., Wiltshire, A., and Zhao, M. S.: Spatiotemporal
616 patterns of terrestrial gross primary production: A review, *Reviews of Geophysics*, 53, 785-818,
617 <https://doi.org/10.1002/2015rg000483>, 2015.

618 Arora, V. K.: Simulating energy and carbon fluxes over winter wheat using coupled land surface and
619 terrestrial ecosystem models, *Agric. For. Meteorol.*, 118, 21-47, [https://doi.org/10.1016/s0168-](https://doi.org/10.1016/s0168-1923(03)00073-x)
620 [1923\(03\)00073-x](https://doi.org/10.1016/s0168-1923(03)00073-x), 2003.

621 Bellouin, N., Quaas, J., Gryspeerdt, E., Kinne, S., Stier, P., Watson-Parris, D., Boucher, O., Carslaw, K.
622 S., Christensen, M., Daniau, A. L., Dufresne, J. L., Feingold, G., Fiedler, S., Forster, P., Gettelman, A.,
623 Haywood, J. M., Lohmann, U., Malavelle, F., Mauritsen, T., McCoy, D. T., Myhre, G., Mulmenstadt, J.,
624 Neubauer, D., Possner, A., Rugenstein, M., Sato, Y., Schulz, M., Schwartz, S. E., Sourdeval, O.,
625 Storelvmo, T., Toll, V., Winker, D., and Stevens, B.: Bounding Global Aerosol Radiative Forcing of
626 Climate Change, *Rev Geophys*, 58, e2019RG000660, <https://doi.org/10.1029/2019RG000660>, 2020.

627 Bloomfield, K. J., Stocker, B. D., Keenan, T. F., and Prentice, I. C.: Environmental controls on the light
628 use efficiency of terrestrial gross primary production, *Global Change Biol*, 29, 1037-1053,
629 <https://doi.org/10.1111/gcb.16511>, 2022.

630 Boucher, O., Servonnat, J., Albright, A. L., Aumont, O., Balkanski, Y., Bastrikov, V., Bekki, S., Bonnet,
631 R., Bony, S., Bopp, L., Braconnot, P., Brockmann, P., Cadule, P., Caubel, A., Cheruy, F., Codron, F.,
632 Cozic, A., Cugnet, D., D'Andrea, F., Davini, P., de Lavergne, C., Denvil, S., Deshayes, J., Devilliers, M.,
633 Ducharme, A., Dufresne, J. L., Dupont, E., Éthé, C., Fairhead, L., Falletti, L., Flavoni, S., Foujols, M. A.,
634 Gardoll, S., Gastineau, G., Ghattas, J., Grandpeix, J. Y., Guenet, B., Guez, L. E., Guilyardi, E.,
635 Guimberteau, M., Hauglustaine, D., Hourdin, F., Idelkadi, A., Joussaume, S., Kageyama, M., Khodri, M.,
636 Krinner, G., Lebas, N., Levavasseur, G., Lévy, C., Li, L., Lott, F., Lurton, T., Luyssaert, S., Madec, G.,
637 Madeleine, J. B., Maignan, F., Marchand, M., Marti, O., Mellul, L., Meurdesoif, Y., Mignot, J., Musat,
638 I., Ottlé, C., Peylin, P., Planton, Y., Polcher, J., Rio, C., Rochetin, N., Rousset, C., Sepulchre, P., Sima,
639 A., Swingedouw, D., Thiéblemont, R., Traore, A. K., Vancoppenolle, M., Vial, J., Vialard, J., Viovy, N.,
640 and Vuichard, N.: Presentation and Evaluation of the IPSL-CM6A-LR Climate Model, *Journal of*
641 *Advances in Modeling Earth Systems*, 12, <https://doi.org/10.1029/2019MS002010>, 2020.

642 Cheruy, F., Ducharme, A., Hourdin, F., Musat, I., Vignon, É., Gastineau, G., Bastrikov, V., Vuichard, N.,
643 Diallo, B., Dufresne, J. L., Ghattas, J., Grandpeix, J. Y., Idelkadi, A., Mellul, L., Maignan, F., Ménégoz,
644 M., Ottlé, C., Peylin, P., Servonnat, J., Wang, F., and Zhao, Y.: Improved Near-Surface Continental

645 Climate in IPSL-CM6A-LR by Combined Evolutions of Atmospheric and Land Surface Physics, *Journal*
646 *of Advances in Modeling Earth Systems*, 12, <https://doi.org/10.1029/2019MS002005>, 2020.

647 Clark, D. B., Mercado, L. M., Sitch, S., Jones, C. D., Gedney, N., Best, M. J., Pryor, M., Rooney, G. G.,
648 Essery, R. L. H., Blyth, E., Boucher, O., Harding, R. J., Huntingford, C., and Cox, P. M.: The Joint UK
649 Land Environment Simulator (JULES), model description - Part 2: Carbon fluxes and vegetation
650 dynamics, *Geoscientific Model Development*, 4, 701-722, <https://doi.org/10.5194/gmd-4-701-2011>,
651 2011.

652 Collins, W. J., Lamarque, J. F., Schulz, M., Boucher, O., Eyring, V., Hegglin, M. I., Maycock, A., Myhre,
653 G., Prather, M., Shindell, D., and Smith, S. J.: AerChemMIP: quantifying the effects of chemistry and
654 aerosols in CMIP6, *Geoscientific Model Development*, 10, 585-607, [https://doi.org/10.5194/gmd-10-](https://doi.org/10.5194/gmd-10-585-2017)
655 [585-2017](https://doi.org/10.5194/gmd-10-585-2017), 2017.

656 Earth System Grid Foundation: Earth System Grid Foundation (2024) [dataset], 2024.

657 Eyring, V., Bony, S., Meehl, G. A., Senior, C. A., Stevens, B., Stouffer, R. J., and Taylor, K. E.: Overview
658 of the Coupled Model Intercomparison Project Phase 6 (CMIP6) experimental design and organization,
659 *Geoscientific Model Development*, 9, 1937-1958, <https://doi.org/10.5194/gmd-9-1937-2016>, 2016.

660 Fang, H. L.: Canopy clumping index (CI): A review of methods, characteristics, and applications, *Agric.*
661 *For. Meteorol.*, 303, 108374, <https://doi.org/10.1016/j.agrformet.2021.108374>, 2021.

662 Gabele, L. M., Sieber, P., Liu, L., and Seneviratne, S. I.: Soil moisture-induced changes in land carbon
663 sink projections in CMIP6, *EGUsphere*, 2025, 1-23, <https://doi.org/10.5194/egusphere-2025-4215>, 2025.

664 Gier, B. K., Schlund, M., Friedlingstein, P., Jones, C. D., Jones, C., Zaehle, S., and Eyring, V.:
665 Representation of the terrestrial carbon cycle in CMIP6, *Biogeosciences*, 21, 5321-5360,
666 <https://doi.org/10.5194/bg-21-5321-2024>, 2024.

667 Gu, L., Baldocchi, D., Verma, S. B., Black, T. A., Vesala, T., Falge, E. M., and Dowty, P. R.: Advantages
668 of diffuse radiation for terrestrial ecosystem productivity, *Journal of Geophysical Research: Atmospheres*,
669 107, ACL 2-1-ACL 2-23, <https://doi.org/10.1029/2001jd001242>, 2002.

670 Gu, L., Baldocchi, D. D., Wofsy, S. C., Munger, J. W., Michalsky, J. J., Urbanski, S. P., and Boden, T. A.:
671 Response of a deciduous forest to the Mount Pinatubo eruption: enhanced photosynthesis, *Science*, 299,
672 2035-2038, <https://doi.org/10.1126/science.1078366>, 2003.

673 Hu, Q., Li, T., Deng, X., Wu, T., Zhai, P., Huang, D., Fan, X., Zhu, Y., Lin, Y., Xiao, X., Chen, X., Zhao,
674 X., Wang, L., and Qin, Z.: Intercomparison of global terrestrial carbon fluxes estimated by MODIS and
675 Earth system models, *Sci. Total Environ.*, 810, 152231, <https://doi.org/10.1016/j.scitotenv.2021.152231>,
676 2022.

677 Huang, M., Piao, S., Ciais, P., Penuelas, J., Wang, X., Keenan, T. F., Peng, S., Berry, J. A., Wang, K.,
678 Mao, J., Alkama, R., Cescatti, A., Cuntz, M., De Deurwaerder, H., Gao, M., He, Y., Liu, Y., Luo, Y.,
679 Myneni, R. B., Niu, S., Shi, X., Yuan, W., Verbeeck, H., Wang, T., Wu, J., and Janssens, I. A.: Air
680 temperature optima of vegetation productivity across global biomes, *Nat Ecol Evol*, 3, 772-779,
681 <https://doi.org/10.1038/s41559-019-0838-x>, 2019.

682 Khatri, P., Hayasaka, T., Holben, B., Tripathi, S. N., Misra, P., Patra, P. K., Hayashida, S., and Dumka,
683 U. C.: Aerosol Loading and Radiation Budget Perturbations in Densely Populated and Highly Polluted
684 Indo-Gangetic Plain by COVID-19: Influences on Cloud Properties and Air Temperature, *Geophys. Res.*
685 *Let.*, 48, e2021GL093796, <https://doi.org/10.1029/2021GL093796>, 2021.

686 Lai, J., Kooijmans, L. M. J., Sun, W., Lombardozzi, D., Campbell, J. E., Gu, L., Luo, Y., Kuai, L., and
687 Sun, Y.: Terrestrial photosynthesis inferred from plant carbonyl sulfide uptake, *Nature*,
688 <https://doi.org/10.1038/s41586-024-08050-3>, 2024.

689 Lasslop, G., Reichstein, M., Papale, D., Richardson, A. D., Arneth, A., Barr, A., Stoy, P., and Wohlfahrt,
690 G.: Separation of net ecosystem exchange into assimilation and respiration using a light response curve
691 approach: critical issues and global evaluation, *Global Change Biol*, 16, 187-208,
692 <https://doi.org/10.1111/j.1365-2486.2009.02041.x>, 2010.

693 Lawrence, D. M., Oleson, K. W., Flanner, M. G., Thornton, P. E., Swenson, S. C., Lawrence, P. J., Zeng,
694 X., Yang, Z.-L., Levis, S., Sakaguchi, K., Bonan, G. B., and Slater, A. G.: Parameterization improvements
695 and functional and structural advances in Version 4 of the Community Land Model, *Journal of Advances
696 in Modeling Earth Systems*, 3, 1-27, <https://doi.org/10.1029/2011ms000045>, 2011.

697 Lawrence, D. M., Fisher, R. A., Koven, C. D., Oleson, K. W., Swenson, S. C., Bonan, G., Collier, N.,
698 Ghimire, B., van Kampenhout, L., Kennedy, D., Kluzek, E., Lawrence, P. J., Li, F., Li, H., Lombardozzi,
699 D., Riley, W. J., Sacks, W. J., Shi, M., Vertenstein, M., Wieder, W. R., Xu, C., Ali, A. A., Badger, A. M.,
700 Bisht, G., van den Broeke, M., Brunke, M. A., Burns, S. P., Buzan, J., Clark, M., Craig, A., Dahlin, K.,
701 Drewniak, B., Fisher, J. B., Flanner, M., Fox, A. M., Gentine, P., Hoffman, F., Keppel-Aleks, G., Knox,
702 R., Kumar, S., Lenaerts, J., Leung, L. R., Lipscomb, W. H., Lu, Y., Pandey, A., Pelletier, J. D., Perket, J.,
703 Randerson, J. T., Ricciuto, D. M., Sanderson, B. M., Slater, A., Subin, Z. M., Tang, J., Thomas, R. Q.,
704 Val Martin, M., and Zeng, X.: The Community Land Model Version 5: Description of New Features,
705 Benchmarking, and Impact of Forcing Uncertainty, *Journal of Advances in Modeling Earth Systems*, 11,
706 4245-4287, <https://doi.org/10.1029/2018MS001583>, 2019.

707 Leung, G. R. and van den Heever, S. C.: Aerosol breezes drive cloud and precipitation increases, *Nat.
708 Commun.*, 14, 2508, <https://doi.org/10.1038/s41467-023-37722-3>, 2023.

709 Li, F., Hao, D., Zhu, Q., Yuan, K., Braghieri, R. K., He, L., Luo, X., Wei, S., Riley, W. J., Zeng, Y., and
710 Chen, M.: Vegetation clumping modulates global photosynthesis through adjusting canopy light
711 environment, *Glob Chang Biol*, 29, 731-746, <https://doi.org/10.1111/gcb.16503>, 2023.

712 Li, W. P., Zhang, Y. W., Shi, X. L., Zhou, W. Y., Huang, A. N., Mu, M. Q., Qiu, B., and Ji, J. J.:
713 Development of Land Surface Model BCC_AVIM2.0 and Its Preliminary Performance in
714 LS3MIP/CMIP6, *Journal of Meteorological Research*, 33, 851-869, <https://doi.org/10.1007/s13351-019-9016-y>, 2019.

716 Liu, Q. Z., Zhang, Z. Y., Fan, M., and Wang, Q.: The Divergent Estimates of Diffuse Radiation Effects
717 on Gross Primary Production of Forest Ecosystems Using Light-Use Efficiency Models, *Geophys. Res.
718 Lett.*, 48, e2021GL093864, <https://doi.org/10.1029/2021GL093864>, 2021.

719 Liu, Z. C., Lang, X. M., and Jiang, D. B.: Impact of stratospheric aerosol intervention geoengineering on
720 surface air temperature in China: a surface energy budget perspective, *Atmos. Chem. Phys.*, 22, 7667-
721 7680, <https://doi.org/10.5194/acp-22-7667-2022>, 2022.

722 Mauritsen, T., Bader, J., Becker, T., Behrens, J., Bittner, M., Brokopf, R., Brovkin, V., Claussen, M.,
723 Crueger, T., Esch, M., Fast, I., Fiedler, S., Flaschner, D., Gayler, V., Giorgetta, M., Goll, D. S., Haak, H.,
724 Hagemann, S., Hedemann, C., Hohenegger, C., Ilyina, T., Jahns, T., Jimenez-de-la-Cuesta, D., Jungclaus,
725 J., Kleinen, T., Kloster, S., Kracher, D., Kinne, S., Kleberg, D., Lasslop, G., Kornbluch, L., Marotzke, J.,
726 Matei, D., Meraner, K., Mikolajewicz, U., Modali, K., Mobis, B., Muller, W. A., Nabel, J., Nam, C. C.
727 W., Notz, D., Nyawira, S. S., Paulsen, H., Peters, K., Pincus, R., Pohlmann, H., Pongratz, J., Popp, M.,
728 Raddatz, T. J., Rast, S., Redler, R., Reick, C. H., Rohrschneider, T., Schemann, V., Schmidt, H., Schnur,
729 R., Schulzweida, U., Six, K. D., Stein, L., Stemmler, I., Stevens, B., von Storch, J. S., Tian, F., Voigt, A.,
730 Vrese, P., Wieners, K. H., Wilkenskjaeld, S., Winkler, A., and Roeckner, E.: Developments in the MPI-M
731 Earth System Model version 1.2 (MPI-ESM1.2) and Its Response to Increasing CO₂, *J Adv Model
732 Earth Syst*, 11, 998-1038, <https://doi.org/10.1029/2018MS001400>, 2019.

733 Mercado, L. M., Bellouin, N., Sitch, S., Boucher, O., Huntingford, C., Wild, M., and Cox, P. M.: Impact
734 of changes in diffuse radiation on the global land carbon sink, *Nature*, 458, 1014-1017,
735 <https://doi.org/10.1038/nature07949>, 2009.

736 Najafi, M. R., Zwiers, F. W., and Gillett, N. P.: Attribution of Arctic temperature change to greenhouse-
737 gas and aerosol influences, *Nature Climate Change*, 5, 246-249, <https://doi.org/10.1038/Nclimate2524>,
738 2015.

739 Nelson, J. A., Walther, S., Jung, M., Gans, F., Kraft, B., Weber, U., Hamdi, Z., Duveiller, G., and Zhang,
740 W.: FLUXCOM-X-BASE [dataset], <https://doi.org/10.18160/5NZG-JMJE>, 2023.

741 Nelson, J. A., Walther, S., Gans, F., Kraft, B., Weber, U., Novick, K., Buchmann, N., Migliavacca, M.,
742 Wohlfahrt, G., Šigut, L., Ibrom, A., Papale, D., Göckede, M., Duveiller, G., Knohl, A., Hörtnagl, L., Scott,
743 R. L., Zhang, W., Hamdi, Z. M., Reichstein, M., Aranda-Barranco, S., Ardö, J., Op de Beeck, M.,
744 Billesbach, D., Bowling, D., Bracho, R., Brümmner, C., Camps-Valls, G., Chen, S., Cleverly, J. R., Desai,
745 A., Dong, G., El-Madany, T. S., Euskirchen, E. S., Feigenwinter, I., Galvagno, M., Gerosa, G., Gielen,
746 B., Goded, I., Goslee, S., Gough, C. M., Heinesch, B., Ichii, K., Jackowicz-Korczynski, M. A.,
747 Klosterhalfen, A., Knox, S., Kobayashi, H., Kohonen, K. M., Korkiakoski, M., Mammarella, I., Mana,
748 G., Marzuoli, R., Matamala, R., Metzger, S., Montagnani, L., Nicolini, G., O'Halloran, T., Ourcival, J.
749 M., Peichl, M., Pendall, E., Ruiz Reverter, B., Roland, M., Sabbatini, S., Sachs, T., Schmidt, M., Schwalm,
750 C. R., Shekhar, A., Silberstein, R., Silveira, M. L., Spano, D., Tagesson, T., Tramontana, G., Trotta, C.,
751 Turco, F., Vesala, T., Vincke, C., Vitale, D., Vivoni, E. R., Wang, Y., Woodgate, W., Yopez, E. A., Zhang,
752 J., Zona, D., and Jung, M.: X-BASE: the first terrestrial carbon and water flux products from an extended
753 data-driven scaling framework, *FLUXCOM-X, EGUsphere*, 2024, 1-51,
754 <https://doi.org/10.5194/egusphere-2024-165>, 2024.

755 Niyogi, D., Chang, H. I., Saxena, V. K., Holt, T., Alapaty, K., Booker, F., Chen, F., Davis, K. J., Holben,
756 B., Matsui, T., Meyers, T., Oechel, W. C., Pielke, R. A., Wells, R., Wilson, K., and Xue, Y.: Direct
757 observations of the effects of aerosol loading on net ecosystem CO₂ exchanges over different landscapes,
758 *Geophys. Res. Lett.*, 31, <https://doi.org/10.1029/2004gl020915>, 2004.

759 Pastorello, G., Trotta, C., Canfora, E., Chu, H., Christianson, D., Cheah, Y. W., Poindexter, C., Chen, J.,
760 Elbashandy, A., Humphrey, M., Isaac, P., Polidori, D., Reichstein, M., Ribeca, A., van Ingen, C., Vuichard,
761 N., Zhang, L., Amiro, B., Ammann, C., Arain, M. A., Ardo, J., Arkebauer, T., Arndt, S. K., Arriga, N.,
762 Aubinet, M., Aurela, M., Baldocchi, D., Barr, A., Beamesderfer, E., Marchesini, L. B., Bergeron, O.,
763 Beringer, J., Bernhofer, C., Berveiller, D., Billesbach, D., Black, T. A., Blanken, P. D., Bohrer, G., Boike,
764 J., Bolstad, P. V., Bonal, D., Bonnefond, J. M., Bowling, D. R., Bracho, R., Brodeur, J., Brummer, C.,
765 Buchmann, N., Burban, B., Burns, S. P., Buysse, P., Cale, P., Cavagna, M., Cellier, P., Chen, S., Chini, I.,
766 Christensen, T. R., Cleverly, J., Collalti, A., Consalvo, C., Cook, B. D., Cook, D., Coursolle, C.,
767 Cremonese, E., Curtis, P. S., D'Andrea, E., da Rocha, H., Dai, X., Davis, K. J., Cinti, B., Grandcourt, A.,
768 Ligne, A., De Oliveira, R. C., Delpierre, N., Desai, A. R., Di Bella, C. M., Tommasi, P. D., Dolman, H.,
769 Domingo, F., Dong, G., Dore, S., Duce, P., Dufrene, E., Dunn, A., Dusek, J., Eamus, D., Eichelmann, U.,
770 ElKhidir, H. A. M., Eugster, W., Ewenz, C. M., Ewers, B., Famulari, D., Fares, S., Feigenwinter, I., Feitz,
771 A., Fensholt, R., Filippa, G., Fischer, M., Frank, J., Galvagno, M., Gharun, M., Gianelle, D., Gielen, B.,
772 Gioli, B., Gitelson, A., Goded, I., Goeckede, M., Goldstein, A. H., Gough, C. M., Goulden, M. L., Graf,
773 A., Griebel, A., Gruening, C., Grunwald, T., Hammerle, A., Han, S., Han, X., Hansen, B. U., Hanson, C.,
774 Hatakka, J., He, Y., Hehn, M., Heinesch, B., Hinko-Najera, N., Hortnagl, L., Hutley, L., Ibrom, A., Ikawa,
775 H., Jackowicz-Korczynski, M., Janous, D., Jans, W., Jassal, R., Jiang, S., Kato, T., Khomik, M., Klatt, J.,
776 Knohl, A., Knox, S., Kobayashi, H., Koerber, G., Kolle, O., Kosugi, Y., Kotani, A., Kowalski, A., Kruijft,

777 B., Kurbatova, J., Kutsch, W. L., Kwon, H., Launiainen, S., Laurila, T., Law, B., Leuning, R., Li, Y.,
778 Liddell, M., Limousin, J. M., Lion, M., Liska, A. J., Lohila, A., Lopez-Ballesteros, A., Lopez-Blanco, E.,
779 Loubet, B., Loustau, D., Lucas-Moffat, A., Luers, J., Ma, S., Macfarlane, C., Magliulo, V., Maier, R.,
780 Mammarella, I., Manca, G., Marcolla, B., Margolis, H. A., Marras, S., Massman, W., Mastepanov, M.,
781 Matamala, R., Matthes, J. H., Mazzenga, F., McCaughey, H., McHugh, I., McMillan, A. M. S., Merbold,
782 L., Meyer, W., Meyers, T., Miller, S. D., Minerbi, S., Moderow, U., Monson, R. K., Montagnani, L.,
783 Moore, C. E., Moors, E., Moreaux, V., Moureaux, C., Munger, J. W., Nakai, T., Neiryneck, J., Nestic, Z.,
784 Nicolini, G., Noormets, A., Northwood, M., Nosetto, M., Nouvellon, Y., Novick, K., Oechel, W., Olesen,
785 J. E., Ourcival, J. M., Papuga, S. A., Parmentier, F. J., Paul-Limoges, E., Pavelka, M., Peichl, M., Pendall,
786 E., Phillips, R. P., Pilegaard, K., Pirk, N., Posse, G., Powell, T., Prasse, H., Prober, S. M., Rambal, S.,
787 Rannik, U., Raz-Yaseef, N., Rebmann, C., Reed, D., Dios, V. R., Restrepo-Coupe, N., Reverter, B. R.,
788 Roland, M., Sabbatini, S., Sachs, T., Saleska, S. R., Sanchez-Canete, E. P., Sanchez-Mejia, Z. M., Schmid,
789 H. P., Schmidt, M., Schneider, K., Schrader, F., Schroder, I., Scott, R. L., Sedlak, P., Serrano-Ortiz, P.,
790 Shao, C., Shi, P., Shironya, I., Siebicke, L., Sigut, L., Silberstein, R., Sirca, C., Spano, D., Steinbrecher,
791 R., Stevens, R. M., Sturtevant, C., Suyker, A., Tagesson, T., Takanashi, S., Tang, Y., Tapper, N., Thom,
792 J., Tomassucci, M., Tuovinen, J. P., Urbanski, S., Valentini, R., van der Molen, M., van Gorsel, E., van
793 Huissteden, K., Varlagin, A., Verfaillie, J., Vesala, T., Vincke, C., Vitale, D., Vygodskaya, N., Walker, J.
794 P., Walter-Shea, E., Wang, H., Weber, R., Westermann, S., Wille, C., Wofsy, S., Wohlfahrt, G., Wolf, S.,
795 Woodgate, W., Li, Y., Zampedri, R., Zhang, J., Zhou, G., Zona, D., Agarwal, D., Biraud, S., Torn, M.,
796 and Papale, D.: The FLUXNET2015 dataset and the ONEFlux processing pipeline for eddy covariance
797 data, *Sci Data*, 7, 225, <https://doi.org/10.1038/s41597-020-0534-3>, 2020.

798 Piao, S., Ciais, P., Friedlingstein, P., Peylin, P., Reichstein, M., Luyssaert, S., Margolis, H., Fang, J., Barr,
799 A., Chen, A., Grelle, A., Hollinger, D. Y., Laurila, T., Lindroth, A., Richardson, A. D., and Vesala, T.: Net
800 carbon dioxide losses of northern ecosystems in response to autumn warming, *Nature*, 451, 49-52,
801 <https://doi.org/10.1038/nature06444>, 2008.

802 Rap, A., Scott, C. E., Reddington, C. L., Mercado, L., Ellis, R. J., Garraway, S., Evans, M. J., Beerling,
803 D. J., MacKenzie, A. R., Hewitt, C. N., and Spracklen, D. V.: Enhanced global primary production by
804 biogenic aerosol via diffuse radiation fertilization, *Nature Geoscience*, 11, 640-+,
805 <https://doi.org/10.1038/s41561-018-0208-3>, 2018.

806 Reick, C. H., Gayler, V., Goll, D., Hagemann, S., Heidkamp, M., Nabel, J. E. M. S., Raddatz, T., Roeckner,
807 E., Schnur, R., and Wilkenskjaeld, S.: JSBACH 3 - The land component of the MPI Earth System Model:
808 documentation of version 3.2, MPI für Meteorologie, <https://doi.org/10.17617/2.3279802>, 2021.

809 Ren, Y. H., Wang, H., Harrison, S. P., Prentice, I. C., Mengoli, G., Zhao, L., Reich, P. B., and Yang, K.:
810 Incorporating the Acclimation of Photosynthesis and Leaf Respiration in the Noah-MP Land Surface
811 Model: Model Development and Evaluation, *Journal of Advances in Modeling Earth Systems*, 17,
812 <https://doi.org/10.1029/2024MS004599>, 2025.

813 Sellar, A. A., Jones, C. G., Mulcahy, J. P., Tang, Y., Yool, A., Wiltshire, A., O'Connor, F. M., Stringer, M.,
814 Hill, R., Palmieri, J., Woodward, S., de Mora, L., Kuhlbrodt, T., Rumbold, S. T., Kelley, D. I., Ellis, R.,
815 Johnson, C. E., Walton, J., Abraham, N. L., Andrews, M. B., Andrews, T., Archibald, A. T., Berthou, S.,
816 Burke, E., Blockley, E., Carslaw, K., Dalvi, M., Edwards, J., Folberth, G. A., Gedney, N., Griffiths, P. T.,
817 Harper, A. B., Hendry, M. A., Hewitt, A. J., Johnson, B., Jones, A., Jones, C. D., Keeble, J., Liddicoat,
818 S., Morgenstern, O., Parker, R. J., Predoi, V., Robertson, E., Siahhaan, A., Smith, R. S., Swaminathan, R.,
819 Woodhouse, M. T., Zeng, G., and Zerroukat, M.: UKESM1: Description and Evaluation of the U.K. Earth
820 System Model, *Journal of Advances in Modeling Earth Systems*, 11, 4513-4558,

821 <https://doi.org/10.1029/2019MS001739>, 2019.

822 Song, Y., Jiao, W., Wang, J., and Wang, L.: Increased Global Vegetation Productivity Despite Rising
823 Atmospheric Dryness Over the Last Two Decades, *Earth's Future*, 10, e2021EF002634,
824 <https://doi.org/10.1029/2021ef002634>, 2022.

825 Tan, Y. H., Wang, Q., and Zhang, Z. Y.: Near-real-time estimation of global horizontal irradiance from
826 Himawari-8 satellite data, *Renewable Energy*, 215, 118994,
827 <https://doi.org/10.1016/j.renene.2023.118994>, 2023.

828 Wang, X., Wu, J., Chen, M., Xu, X., Wang, Z., Wang, B., Wang, C., Piao, S., Lin, W., Miao, G., Deng,
829 M., Qiao, C., Wang, J., Xu, S., and Liu, L.: Field evidences for the positive effects of aerosols on tree
830 growth, *Glob Chang Biol*, 24, 4983-4992, <https://doi.org/10.1111/gcb.14339>, 2018.

831 Wang, Z., Chen, W., Piao, J., Cai, Q., Chen, S., Xue, X., and Ma, T.: Synergistic effects of high
832 atmospheric and soil dryness on record-breaking decreases in vegetation productivity over Southwest
833 China in 2023, *npj Climate and Atmospheric Science*, 8, <https://doi.org/10.1038/s41612-025-00895-3>,
834 2025.

835 Wu, D., Yuan, T., Zhang, J., Zhang, Z., Zhang, D., Zhang, B., Liu, J., Pu, W., and Wang, X.: Contrasting
836 Responses of Smoke Dispersion and Fire Emissions to Aerosol-Radiation Interaction during the Largest
837 Australian Wildfires in 2019-2020, *Environ Sci Technol*, 59, 1724-1736,
838 <https://doi.org/10.1021/acs.est.4c12034>, 2025.

839 Wu, T. W., Zhang, F., Zhang, J., Jie, W. H., Zhang, Y. W., Wu, F. H., Li, L., Yan, J. H., Liu, X. H., Lu, X.,
840 Tan, H. Y., Zhang, L., Wang, J., and Hu, A. X.: Beijing Climate Center Earth System Model version 1
841 (BCC-ESM1): model description and evaluation of aerosol simulations, *Geoscientific Model
842 Development*, 13, 977-1005, <https://doi.org/10.5194/gmd-13-977-2020>, 2020.

843 Yu, Q. and Huang, Y.: Distributions and Trends of the Aerosol Direct Radiative Effect in the 21st Century:
844 Aerosol and Environmental Contributions, *Journal of Geophysical Research: Atmospheres*, 128,
845 <https://doi.org/10.1029/2022jd037716>, 2023.

846 Yue, X. and Unger, N.: Aerosol optical depth thresholds as a tool to assess diffuse radiation fertilization
847 of the land carbon uptake in China, *Atmos. Chem. Phys.*, 17, 1329-1342, [https://doi.org/10.5194/acp-17-
848 1329-2017](https://doi.org/10.5194/acp-17-1329-2017), 2017.

849 Zhang, H. W., Li, L. H., Song, J., Akhter, Z. H., and Zhang, J. J.: Understanding aerosol-climate-
850 ecosystem interactions and the implications for terrestrial carbon sink using the Community Earth
851 System Model, *Agric. For. Meteorol.*, 340, 109625, <https://doi.org/10.1016/j.agrformet.2023.109625>,
852 2023a.

853 Zhang, L., Li, J., Jiang, Z. J., Dong, Y. M., Ying, T., and Zhang, Z. Y.: Clear-Sky Direct Aerosol Radiative
854 Forcing Uncertainty Associated with Aerosol Optical Properties Based on CMIP6 Models, *Journal of
855 Climate*, 35, 3007-3019, <https://doi.org/10.1175/Jcli-D-21-0479.1>, 2022.

856 Zhang, Y., Ciais, P., Boucher, O., Maignan, F., Bastos, A., Goll, D., Lurton, T., Viovy, N., Bellouin, N.,
857 and Li, L.: Disentangling the Impacts of Anthropogenic Aerosols on Terrestrial Carbon Cycle During
858 1850-2014, *Earths Future*, 9, e2021EF002035, <https://doi.org/10.1029/2021EF002035>, 2021a.

859 Zhang, Y., Goll, D., Bastos, A., Balkanski, Y., Boucher, O., Cescatti, A., Collier, M., Gasser, T., Ghattas,
860 J., Li, L., Piao, S., Viovy, N., Zhu, D., and Ciais, P.: Increased Global Land Carbon Sink Due to Aerosol-
861 Induced Cooling, *Global Biogeochem. Cycles*, 33, 439-457, <https://doi.org/10.1029/2018gb006051>,
862 2019.

863 Zhang, Y., Bastos, A., Maignan, F., Goll, D., Boucher, O., Li, L., Cescatti, A., Vuichard, N., Chen, X. Z.,
864 Ammann, C., Arain, M. A., Black, T. A., Chojnicki, B., Kato, T., Mammarella, I., Montagnani, L.,

865 Roupsard, O., Sanz, M. J., Siebicke, L., Urbaniak, M., Vaccari, F. P., Wohlfahrt, G., Woodgate, W., and
866 Ciais, P.: Modeling the impacts of diffuse light fraction on photosynthesis in ORCHIDEE (v5453) land
867 surface model, *Geoscientific Model Development*, 13, 5401-5423, [https://doi.org/10.5194/gmd-13-](https://doi.org/10.5194/gmd-13-5401-2020)
868 [5401-2020](https://doi.org/10.5194/gmd-13-5401-2020), 2020.

869 Zhang, Z.: Post-processing scripts for "Ecosystem Climate Sensitivities Drive the Divergence in Aerosol-
870 Induced Carbon Uptake Across CMIP6 Models", Zenodo [code],
871 <https://doi.org/10.5281/zenodo.18396247>, 2026.

872 Zhang, Z., Xiong, J., Fan, M., Tao, M., Wang, Q., and Bai, Y.: Satellite-observed vegetation responses to
873 aerosols variability, *Agric. For. Meteorol.*, 329, 109278, <https://doi.org/10.1016/j.agrformet.2022.109278>,
874 2023b.

875 Zhang, Z. Y., Liu, Q. Z., Ruan, Y. C., and Tan, Y. H.: Estimation of aerosol radiative effects on terrestrial
876 gross primary productivity and water use efficiency using process-based model and satellite data,
877 *Atmospheric Research*, 247, 105245, <https://doi.org/10.1016/j.atmosres.2020.105245>, 2021b.

878 Zhang, Z. Y., Fan, M., Tao, M. H., Tan, Y. H., and Wang, Q.: Large Divergence of Satellite Monitoring
879 of Diffuse Radiation Effect on Ecosystem Water-Use Efficiency, *Geophys. Res. Lett.*, 50,
880 e2023GL106086, <https://doi.org/10.1029/2023GL106086>, 2023c.

881 Zhou, H., Yue, X., Dai, H. B., Geng, G. N., Yuan, W. P., Chen, J. Q., Shen, G. F., Zhang, T. Y., Zhu, J.,
882 and Liao, H.: Recovery of ecosystem productivity in China due to the Clean Air Action plan, *Nature*
883 *Geoscience*, 17, <https://doi.org/10.1038/s41561-024-01586-z>, 2024.

884